

OPTICAL MODEL ANALYSIS OF $p + {}^6\text{He}$ SCATTERING OVER A WIDE RANGE OF ENERGY

Zakaria M. M. Mahmoud^a, Awad A. Ibraheem^{b, c, 1}, M. El-Azab Farid^d

^a Sciences Department, New-Valley Faculty of Education, Assiut University, Egypt

^b Physics Department, Al-Azhar University, Assiut, Egypt

^c Physics Department, King Khalid University, Abha, Saudi Arabia

^d Physics Department, Assiut University, Assiut, Egypt

Optical model analysis of proton elastic scattering from ${}^6\text{He}$ has been carried out for eight sets of elastic scattering data at energies of 24.5, 25.0, 36.2, 38.3, 40.9, 41.6, 71.0 and 82.3 MeV/nucleon, respectively. The vector analyzing power and differential cross section for the elastic scattering of ${}^6\text{He}$ nucleus from polarized protons at 71 MeV have been analyzed in the framework of the optical model potential. The data are, first, analyzed in terms of phenomenological potentials using the Woods–Saxon form for the real and imaginary parts supplemented by a spin-orbit potential of Thomas form. The analysis has been then performed using microscopic single folded complex potentials.

Проводится анализ упругого рассеяния протонов на ${}^6\text{He}$ для восьми энергий рассеяния, 24,5, 25,0, 36,2, 38,3, 40,9, 41,6, 71,0 и 82,3 МэВ/нуклон соответственно, в рамках оптической модели. Векторная анализирующая способность и дифференциальное сечение упругого рассеяния ядер ${}^6\text{He}$ с поляризованными протонами с энергией 71 МэВ анализируется с использованием оптического потенциала. Экспериментальные данные рассматриваются в терминах феноменологического потенциала с использованием формы Вудса–Саксона для реальной части потенциала и формы спин-орбитального потенциала формы Томаса для мнимой части. Анализ проводится с использованием микроскопического одномерного комплексного потенциала.

PACS: 25.70.Bc; 24.10.Ht; 27.20.+n; 21.60.Gx

INTRODUCTION

Over the last decades, since the discovery of the «*halo*» phenomenon in nuclear physics [1], the detailed study of unstable (halo) nuclei has been at the forefront of nuclear physics research. The halo structure refers to highly neutron-rich (*n*-rich) or proton-rich (*p*-rich) light nuclei that lie, respectively, near the neutron- or proton-drip line and hence are totally «unstable» systems. A number of such nuclei have now become available, both as the primary and secondary beams with various low, intermediate and high energies, called the radioactive nuclear beams. With the advent of radioactive nuclear beams and the discovery that nuclear matter, under certain conditions, may present a halo structure, a renewed interest

¹E-mail: awad_ah_eb@hotmail.com

has surged in the investigation of sizes and radial shapes of nuclei. In the case of light n -rich nuclei, this new halo structure is composed of an extended low-density distribution of loosely bound valence neutrons (*halo*) surrounding a core consisting of the majority of the nucleons. With these new radioactive beams, a new degree of freedom, the isospin, is now currently investigated to improve that knowledge and find new phenomena and properties of the nuclear matter. The structures of these nuclei are found to be different from the earlier known structures of nuclei at or near the β -stability line, and are referred to as halo structures.

The ${}^6\text{He}$ nucleus is the prototypical example of a Borromean two-neutron halo nucleus; that is, the nucleus consists of three subsystems (a tightly bound ${}^4\text{He}$ core and two valence neutrons) and none of its binary subsystems has a bound state. The two valence neutrons extend well beyond the ${}^4\text{He}$ core with a separation energy $S_{2n} = 0.975$ MeV [2]. The observed sudden rise in the measured interaction cross section in these nuclei has been attributed to the corresponding large increase in the nuclear root-mean-square radius [1]. Due to the very small separation energy of the last or the valence nucleons of these nuclei, the correct description of their wave functions plays a crucial role in the theoretical description of the scattering and reaction processes [3].

Considerable experimental and theoretical efforts have been devoted to the understanding of the structure of halo nuclei [3–12]. Traditionally, proton scattering has been one of the best means by which the matter densities of the nucleus may be studied. Therefore, in order to investigate the structure of ${}^6\text{He}$, several elastic scattering and interaction cross sections measurements have been performed for the $p + {}^6\text{He}$ reaction at energies of 721 [13], 717 [14], 297 [15], 151 [16, 17], 71 [8, 12, 18], 41.6 [8, 19], 40.9 [8, 20], 38.3 [21], 36 [23] and 24.5 [23, 24] MeV/nucleon. These data have been analyzed either in the framework of the Glauber diffraction theory [25, 26] or using the standard optical model through the single folding (SF) approach based upon the energy- and density-dependent JLM [21, 22, 24], the SBM [27] or the DDM3Y [28] effective nucleon–nucleon (NN) interactions. However, due to the low intensities of the available exotic beams, it is only recently that the inelastic scattering and transfer reactions on light particles could be undertaken to probe deeply the structure of these nuclei, i.e., to acquire further insight into the radial density distribution pertinent to these exotic nuclei [29]. The angular distributions of $p + {}^6\text{He}$ inelastic scattering to the first 2^+ excited state at 1.87 MeV have been measured and analyzed using the SF optical potential at 24.5 and 40.9 MeV/nucleon [24, 20, 30]. In spite of this fair amount of earlier work performed to examine the sensitivity of the elastic scattering data to the physical structure of the exotic helium nucleus, there is not full agreement in the literature to the strength of sensitivity of the elastic proton–nucleus differential cross section at intermediate energies to the structure calculation of the target nucleus ${}^6\text{He}$.

On the other hand, spin observables in scattering experiments have been rich sources for understanding nuclear structure and reactions. Recently, the analyzing power of an unstable beam of ${}^6\text{He}$ on a polarized proton target at an energy of 71 MeV/nucleon was measured for the first time [31]. It was found that at this energy the polarization changes sign from positive to negative at around 50° , which is in contradiction with some theoretical predictions [27, 32]. From the optical model analysis [31], it was implied that the $p - {}^6\text{He}$ spin-orbit potential might extend to a larger radius compared with the $p - {}^6\text{Li}$ case. In a recent theoretical study [33] of the same reaction, the elastic differential cross section and analyzing power observables at 297 MeV/nucleon were calculated using the impulse approximation to the single scattering term of the multiple scattering expansion of the optical potential. They

found that the polarization observable for $p + {}^6\text{He}$ changes sign from positive to negative at around 30° , and that the analyzing power for the $p + {}^4,6\text{He}$ reactions are very similar. They [33], also, claim that an extended neutron distribution cannot be responsible for the spin-orbit radius.

Microscopic models now exist that can predict results of both elastic and inelastic scattering reactions. When good detailed specification of the nucleon structure of the nucleus is used, those predictions usually agree very well with observations both in shape and in magnitude. Thus, it is evident that a priori information on the halo structure of a nucleus is of vital importance for the theoretical treatment of these weakly bound nuclei [34]. In a very recent study, Uesaka et al. [35] and Sakaguchi et al. [12] presented an accurate measurement of the vector analyzing power for the $p + {}^6\text{He}$ elastic scattering at 71 MeV/nucleon. There was used, for the first time, a newly developed polarized proton solid target operated in a low magnetic field and at high temperature. The angular distribution of the elastic scattering differential cross section was also measured at angular range ($42\text{--}87^\circ$) larger than that ($20\text{--}49^\circ$) measured in [18]. In order to obtain theoretical reproduction of the observed data, they [12, 35] employed several (phenomenological, semimicroscopic and fully microscopic) optical potential representations. It was concluded that the spin-orbit potential for ${}^6\text{He}$ is characterized by a shallow and long-ranged shape compared with the global systematic of stable nuclei. This may resemble the diffuse density of the n -rich ${}^6\text{He}$ nucleus. However, the obtained match to the data, in particular the analyzing power at large angles, was not perfect. This may indicate limitation of the structure model and/or contribution of unaccounted reaction mechanisms that influence the larger momentum transfer results [12].

The main aim of the present work is to calculate differential cross sections of elastic ${}^6\text{He} + p$ scattering at different energies studying the possibility to describe the existing experimental data with as minimal number of fitting parameters as possible. First, a phenomenological optical potential of square Woods–Saxon (WS) potential supplied with a Thomas form for the spin-orbit potential was used to describe the experimental data. Second, the single folding (SF) procedure is used to construct the real part of the optical potential (OP). For the construction of the folded potential, two main ingredients are required: (a) an effective nucleon–nucleon (NN) interaction in-medium, allowing for the mean field as well as Pauli blocking effects; and (b) a credible model of structure for the nucleus that is nucleon-based. For the effective interaction the density- and isospin-dependent M3Y effective interaction is used. For this kind of isospin-dependent effective interaction, the real folded potential receives contributions from both isoscalar and isovector components. Usually, in the usage of the complex optical model potential, for analyses of the differential cross sections, their imaginary part and the spin-orbit terms are determined in a phenomenological way.

1. THEORETICAL FORMALISM

Usually, the real part of the nucleon–nucleus optical potential is assumed to be a result of an SF of the effective NN potential with the nuclear density, i.e., this is a particular case of the double folding (DF) [36] in which a $\delta(r_1)$ function has to be used for the density of the incoming particle $\rho_1(r_1)$. The beauty of the folding model lies in the fact that it directly links the density profile of the nucleus with the elastic scattering cross sections. Formally, the SF

potential is given as

$$V(R) = \int \rho_2(r_2) v_{D(\text{EX})}(|\mathbf{s}|, \rho, E) d^3r_2, \quad (1)$$

where $\mathbf{s} = \mathbf{R} - \mathbf{r}_2$. Exotic nuclei usually have nonzero isospin and it is necessary to make explicit the isospin degrees of freedom. For that reason the present calculations have been performed using $v_{D(\text{EX})}(|\mathbf{s}|, \rho, E)$, inside the integral of Eq. (1) for the SF procedure, as the DDM3Y effective [37] interaction given by

$$v_{D(\text{EX})}(|\mathbf{s}|, \rho, E) = v_{\text{IS}}^{D(\text{EX})}(|\mathbf{s}|, \rho, E) + v_{\text{IV}}^{D(\text{EX})}(|\mathbf{s}|, \rho, E), \quad (2)$$

where $v_{\text{IS}}^{D(\text{EX})}(|\mathbf{s}|, \rho, E)$ and $v_{\text{IV}}^{D(\text{EX})}(|\mathbf{s}|, \rho, E)$ are the isoscalar and isovector components of the effective nucleon–nucleon interaction. A realistic separable energy and density-dependent DDM3Y of the following form has been used:

$$v_{\text{IS}}^{D(\text{EX})}(|\mathbf{s}|, \rho, E) = g(E) F_{\text{IS}}^{D(\text{EX})}(\rho_2) v_{00}^{D(\text{EX})}(|\mathbf{s}|), \quad (3)$$

$$v_{\text{IV}}^{D(\text{EX})}(|\mathbf{s}|, \rho, E) = g(E) F_{\text{IV}}^{D(\text{EX})}(\rho_2) v_{01}^{D(\text{EX})}(|\mathbf{s}|). \quad (4)$$

The explicit radial strengths of the isoscalar (IS) and isovector (IV) components of the M3Y interaction based on the G -matrix of the Reid NN potential are given in the following form [38]:

$$v_{00}^D(|\mathbf{s}|) = 7999 \frac{e^{-4|\mathbf{s}|}}{4|\mathbf{s}|} - 2134 \frac{e^{-2.5|\mathbf{s}|}}{2.5|\mathbf{s}|}, \quad (5)$$

$$v_{00}^{\text{EX}}(|\mathbf{s}|) = -J_{00}(E) \delta(|\mathbf{s}|) = -276(1 - 0.005E/A_P), \quad (6)$$

$$v_{01}^D(|\mathbf{s}|) = -4886 \frac{e^{-4|\mathbf{s}|}}{4|\mathbf{s}|} + 1176 \frac{e^{-2.5|\mathbf{s}|}}{2.5|\mathbf{s}|}, \quad (7)$$

$$v_{01}^{\text{EX}}(|\mathbf{s}|) = J_{01}(E) \delta(|\mathbf{s}|) = 228(1 - 0.005E/A_P). \quad (8)$$

Equations (6) and (8) mean that the knock on exchange potential is treated approximately by adding a zero-range pseudopotential [38]. This zero-range approximation has been used with some success in the DF model calculations of the heavy ions (HI) optical potential at low energies [36] where the data are sensitive only to the OP at the surface (near the strong absorption radius), it has been shown to be inadequate [39] in the case of rainbow scattering where the data are sensitive to the real OP over a wider radial domain. The $g(E)$ in Eqs. (3) and (4) represents energy-dependent factor (scaling factor) which takes into account the empirical energy dependence of the nucleon–nucleus optical potential. This scale factor for Reid effective NN interaction takes the form [37]

$$g(E) = 1 - 0.0025E/A_P, \quad (9)$$

where E is the incident particle energy, while A_P is the projectile mass number. The $F_{\text{IS}}^{D(\text{EX})}$ is the realistic density-dependent factor which is included to reproduce the saturation properties of symmetric nuclear matter, while the factor $F_{\text{IV}}^{D(\text{EX})}$ is to reproduce the empirical symmetry energy and so to construct a realistic equation of state for asymmetric nuclear matter. The functional forms of these density-dependent factors are

$$F_{\text{IS,IV}}^{D(\text{EX})}(\rho_2) = C_{\text{IS,IV}}(1 - \gamma\rho), \quad (10)$$

$C_{\text{IS}} = 1.2253$, $C_{\text{IV}} = 0.7597$, $\gamma = 1.5124 \text{ fm}^3$. Through this density dependence the DDM3Y is denoted as BDM3Y1. From Eq. (1) to (10) the direct part of the Re-OP (V_D) has the following form of the IS and IV contributions, correspondingly:

$$V_{\text{IS}}^D(R) = g(E) \int \rho_2(r_2) F(\rho_2) v_{00}^D(|\mathbf{s}|) d^3 r_2, \quad (11)$$

$$V_{\text{IV}}^D(R) = g(E) \int \delta\rho_2(r_2) F(\rho_2) v_{01}^D(|\mathbf{s}|) d^3 r_2, \quad (12)$$

$$\rho_2(r_2) = \rho_{2,p}(r_{2,p}) + \rho_{2,n}(r_{2,n}), \quad (13)$$

$$\delta\rho_2(r_2) = \rho_{2,p}(r_{2,p}) - \rho_{2,n}(r_{2,n}). \quad (14)$$

Here $\rho_{2,p}(r_{2,p})$ and $\rho_{2,n}(r_{2,n})$ are the proton and neutron densities in the target nucleus. We consider a density for ${}^6\text{He}$, which is described with a realistic wave function obtained by the variational Monte Carlo (VMC) wave function used in [14, 40]. This density is composed of ten Gaussian terms as

$$\rho(r) = \sum_{k=1}^{10} (P_k + N_k) \exp(-A_k \cdot r^2). \quad (15)$$

The parameters P_k , N_k and A_k are listed in Table 1. The corresponding rms radii from the VMC wave function density are 2.56, 1.96 and 2.81 fm for nucleon, proton and neutron distributions, respectively.

Table 1. Parameters of the VMC density in Eq. (15)

k	P_k	N_k	A_k
1	$-4.777580124879105 \cdot 10^{-3}$	$-7.022185461489483 \cdot 10^{-3}$	4.0
2	$0.929250185852335 \cdot 10^{-2}$	$2.859012640320818 \cdot 10^{-2}$	2.56
3	$-0.166091230435732 \cdot 10^{-2}$	$0.579676566914048 \cdot 10^{-2}$	1.6384
4	0.230728830390548	$-5.484897586013483 \cdot 10^{-2}$	1.048576
5	-0.177513962911145	$9.683921866054336 \cdot 10^{-2}$	0.67108864
6	0.17863413483804	$-4.977104280767115 \cdot 10^{-2}$	0.4294967296
7	$-4.037779402389877 \cdot 10^{-2}$	0.101382894392589	0.274877906944
8	$2.248885252174397 \cdot 10^{-2}$	$-2.450757473603717 \cdot 10^{-2}$	0.17592186044416
9	$-6.644139893014976 \cdot 10^{-3}$	$1.667264722270956 \cdot 10^{-2}$	0.112589990684262
10	$1.058642564729591 \cdot 10^{-3}$	$7.720490110559399 \cdot 10^{-4}$	$0.205759403792794 \cdot 10^{-2}$

Using Eqs. (1)–(14), one can obtain the following forms of the direct part of the IS Re-OP expressed by integrals in the coordinate and momentum space, correspondingly:

$$V_{\text{IS}}^D(R) = C_{\text{IS}} g(E) \int [\rho_2(r_2) - \gamma \tilde{\rho}_2(r_2)] v_{00}^D(|\mathbf{s}|) d^3 r_2, \quad (16)$$

$$V_{\text{IS}}^D(R) = \frac{C_{\text{IS}} g(E)}{2\pi^2} \int_0^\infty [\rho_2(q) - \gamma \tilde{\rho}_2(q)] v_{00}^D(q) j_0(qr) q^2 dq, \quad (17)$$

where $\tilde{\rho}_2(r_2)$ is given as

$$\tilde{\rho}_2(r_2) = \rho_2^2(r_2). \quad (18)$$

Similarly, exchanging $\rho_2(r_2)$ by $\delta\rho_2(r_2)$ (Eq. (14)), one can obtain the IV part V_{IV}^D of the direct part of Re-OP as

$$V_{IV}^D(R) = C_{IV}g(E) \int [\delta\rho_2(r_2) - \gamma\delta\tilde{\rho}_2(r_2)] v_{01}^D(|\mathbf{s}|) d^3r_2, \quad (19)$$

$$V_{IV}^D(R) = \frac{C_{IV}g(E)}{2\pi^2} \int_0^\infty [\delta\rho_2(r_2) - \gamma\delta\tilde{\rho}_2(r_2)] v_{01}^D(q) j_0(qr) q^2 dq, \quad (20)$$

where $\delta\tilde{\rho}_2(r_2)$ is given as

$$\delta\tilde{\rho}_2(r_2) = [\delta\rho_2(r_2)]^2. \quad (21)$$

The Fourier transforms of $\rho_2(r_2)$, $\delta\rho_2(r_2)$, $\tilde{\rho}_2(r_2)$, $\delta\tilde{\rho}_2(r_2)$, $v_{00}^D(|\mathbf{s}|)$ and $v_{01}^D(|\mathbf{s}|)$ are given from the following relation:

$$f(q) = \int e^{iqr} f(r) d^3r = 4\pi \int_0^\infty f(r) j_0(qr) r^2 dr. \quad (22)$$

The $j_0(qr)$ is the spherical Bessel of order zero. The exchange part of the Re-OP Eqs. (6) and (8) makes it easy to compute in coordinate space because of the presence of delta functions.

2. RESULTS AND DISCUSSION

We perform our calculations on the cross section and analyzing power (at 71 MeV) of $p + {}^6\text{He}$ elastic scattering using phenomenological optical model potentials and the single folded potential. A search for the phenomenological nuclear potential parameters as well as for the normalization parameter for the single folded potential is carried out using the optical model code HERMES [41]. Best fits are obtained by minimizing χ^2 , where

$$\chi^2 = \frac{1}{N} \sum_{i=1}^N \left(\frac{\sigma_{\text{cal}}(\theta_i) - \sigma_{\text{exp}}(\theta_i)}{\Delta\sigma_{\text{exp}}(\theta_i)} \right)^2, \quad (23)$$

where $\sigma_{\text{cal}}(\theta_i)$ and $\sigma_{\text{exp}}(\theta_i)$ are the calculated and experimental cross sections, respectively, at angle, θ_i $\Delta\sigma_{\text{exp}}(\theta_i)$ is the experimental error and N is the number of data points. An average value of 10% is used for the experimental errors of all considered data.

2.1. Phenomenological Analysis. Optical-model analysis of proton elastic scattering from ${}^6\text{He}$ has been carried out for 8 sets of scattering data at energies of 24.5, 25.0, 36.2, 38.3, 40.9, 41.6, 71.0, 82.3 MeV [40], respectively. These data have, in general, been analyzed in terms of an optical model in which the interaction is represented as the scattering of a point particle (proton) by a potential of the standard form,

$$U_{\text{op}}(R) = -V_0 F_r^N(R) - iW_{\text{iv}} F_i^M(R) + 4iaW_{\text{is}} \frac{d}{dR} F_i^M(R) + \frac{2}{R} [V_{\text{so}} + iW_{\text{so}}] \frac{dF_{\text{so}}(R)}{dR} L\sigma_p + U_c(R), \quad (24)$$

where the first term is volume real part of the optical potential $U(R) = -V_0 F_r^N(R)$, the second part is the imaginary potential and usually represented by two terms, volume $W_v(R) = W_{iv} F_i^M(R)$ and surface $W_s(R) = 4aW_{is} \frac{d}{dR} F_i^M(R)$ ones. The third part is the spin-orbit potential (real and imaginary) and in general, it takes the Thomas form. The functional form of the radial form factors $F_k^j(R)$ are usually of WS form, $F_k^j(R) = \left[1 + \exp\left(\frac{R - R_k}{a_k}\right) \right]^{-j}$, $R_k = r_k A^{1/3}$ ($k = r$ for real, i for imaginary, so for spin-orbit potentials, respectively), raised to power j . The L is the relative angular momentum between the proton and ${}^6\text{He}$ nucleus and σ_p is the Pauli spin operator of the proton. The last part, $U_c(R)$, is the Coulomb potential due to a uniform distribution of appropriate size (radius $R_c = r_{0c} A^{1/3}$) and total charge,

$$U_c(R) = \begin{cases} \frac{2e^2}{R}, & R > R_c, \\ \frac{2e^2}{2R_c} \left[3 - \left(\frac{R}{R_c}\right)^2 \right], & R \leq R_c, \end{cases} \quad (25)$$

r_{0c} is fixed at 1.3 fm. We aim in the present analysis to get or extract OP for $p + {}^6\text{He}$ elastic scattering over the considered energy range. For this purpose the usual WS and square WS potentials for the real and imaginary potentials supplied with spin-orbit potential of Thomas form are used. The OP of the usual WS is denoted as Set-1. In this set the shape parameters of both the real and imaginary parts are different and fixed with energy. The OP denoted as Set-2 is of square WS form. The shape parameters of this set are also different for both real and imaginary potentials and fixed with energy as Set-1. The OP denoted as Set-3 is of square WS form but the shape parameters of both the real and imaginary potentials are the same. The shape parameters of spin-orbit potential for these sets are chosen according to the best fitting of the analyzing power data at 71 MeV incident energy. The shape parameters of spin-orbit potential of Set-1 and Set-2 are $r_{so} = 1.248$ fm and $a_{so} = 0.910$ fm. For Set-3 these parameters take the values $r_{so} = 1.301$ fm and $a_{so} = 1.032$ fm. In Fig. 1, the calculations of the observables made with the OPs of Sets-1, 2, and 3 are shown together with the experimental data. The results of these calculations are collected in Table 1. Calculations with Sets-1, 2 and 3 are shown in Fig. 1 by solid, dashed and dash-dotted lines, respectively. The calculations with all the potential sets reproduce both $d\sigma/d\Omega$ and A_y at 71 MeV incident energy over the whole angular region except for the most backward data point of A_y . In these calculations, real spin-orbit potentials are used in Sets-1 and 2 where real and imaginary spin-orbit potentials are used in Set-3. From Table 1 it is shown that addition of surface imaginary potential for the three sets is needed to reproduce the data. Also, it is shown that the real, imaginary and spin-orbit potentials have no clear energy dependence. This may be attributed to the effect of the breakup of the ${}^6\text{He}$ nucleus or to the enhancement of the coupling to the continuum which leads to a greater influence on the nuclear OP of $p + {}^6\text{He}$ system [21].

The calculations based on Sets-1 and 2 result in appreciable similar $d\sigma/d\Omega$ and A_y data as shown in Fig. 1. The calculations based on Set-3 gave $d\sigma/d\Omega$ and A_y different from that of Sets-1 and 2. The calculations of Sets-1 and 2 are near to reproduce the data more than that of Set-3. From all of these calculations it is shown that the phenomenological optical model analyses suggest that the A_y data can be reproduced with a shallow and long-ranged spin-orbit

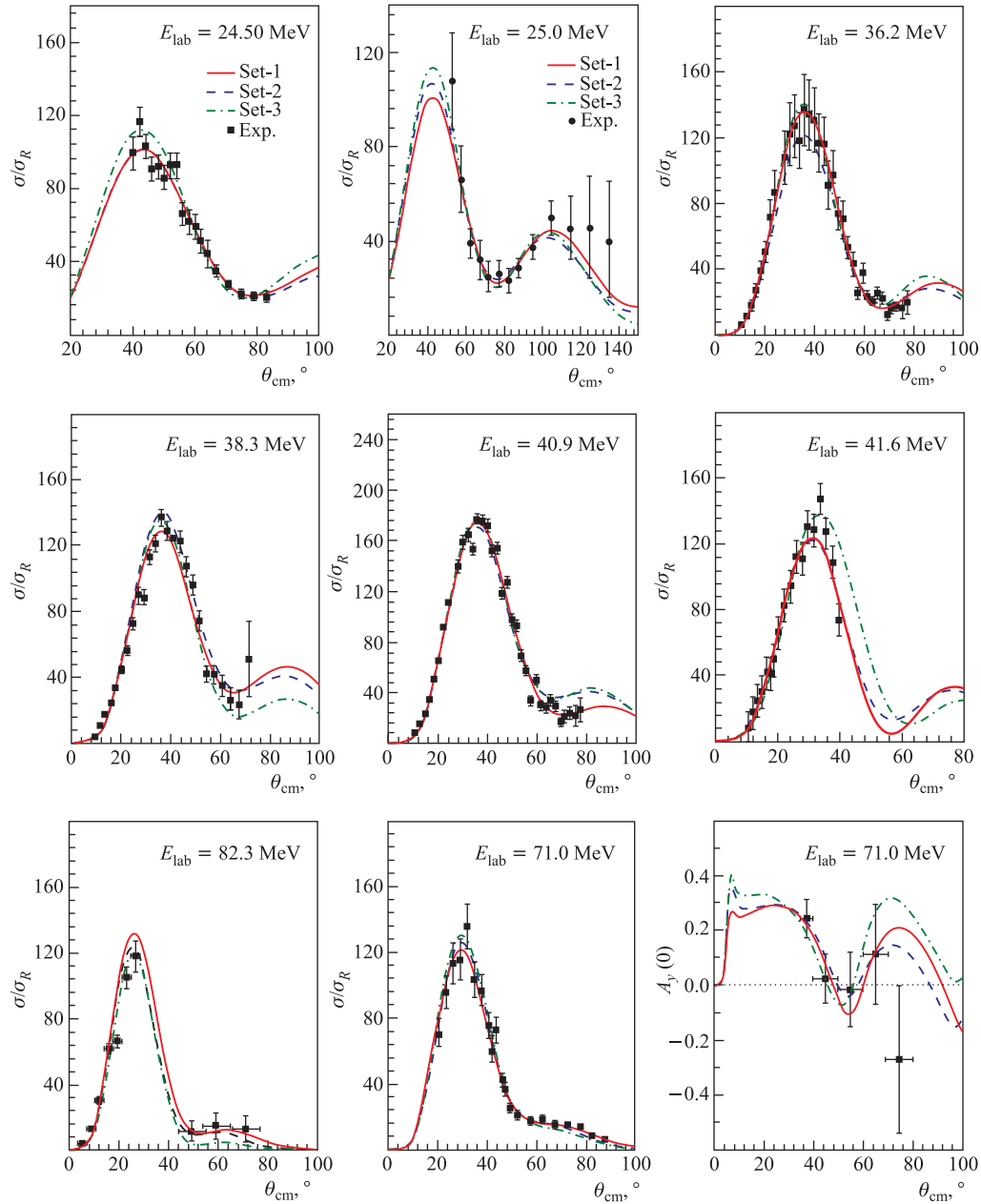


Fig. 1. The angular distribution of elastic $p + {}^6\text{He}$ scattering differential cross section, σ , with respect to Rutherford (Coulomb) cross section, σ_R , at 24.5, 25.0, 36.2, 38.3, 40.9, 41.6, 71.0, 82.3 MeV deduced using phenomenological WS potentials in comparison with measured data

potential, as is clear from Table 1. The phenomenological analysis indicates that the spin-orbit potential between a proton and ${}^6\text{He}$ is characterized by long-ranged radial dependence. Intuitively, these characteristics can be understood from the diffused density distribution of ${}^6\text{He}$. Also, from the table it is clear that the range of the spin-orbit potential for $p + {}^6\text{He}$ scattering is larger than that of the real and imaginary potentials.

2.2. Single Folding Analysis. Usually the real part of the optical model potential is obtained using the folding model. In this calculation, the SF procedure (Eq.(1)) is used to obtain the real part of the OP. The imaginary part is treated phenomenologically either by using the WS forms or by normalizing the SF potential by an imaginary normalization factor N_i . The spin-orbit part is also treated phenomenologically by using the usual Thomas form. The elastic scattering data of $p + {}^6\text{He}$ system have been analyzed using this real folded potential over the energy range considered above. The calculations based on the real SF potential supplied with imaginary potential of WS form are denoted as SFWS1 in both Fig.2 and Table 2. The calculations based on real folded and imaginary potential of square WS are denoted as SFWS2 and SFWS3. In Table 2 it is shown that the shape parameters of the spin-orbit potentials of SFWS1 and SFWS3 are the same and different from that of SFWS2. The shape parameters of spin-orbit potentials used with SFWS1, 3 are $r_{\text{so}} = 1.248$ fm, $a_{\text{so}} = 0.910$ fm with root-mean-square (rms) radius $\langle r_{\text{so}}^2 \rangle^{1/2} = 3.612$ fm. The shape parameters of spin-orbit potentials used with SFWS2 are $r_{\text{so}} = 1.118$ fm, $a_{\text{so}} = 1.134$ fm with rms radius $\langle r_{\text{so}}^2 \rangle^{1/2} = 3.990$ fm. From the figures it is seen that all the potential sets (SFWS1, 2 and 3) reproduce the elastic scattering data equally well except at 38.3, 40.9 and 82.3 MeV. For the energy 38.3 MeV the calculations based on the three sets are very similar up to an angle of around 57° and then deviate. The set SFWS1 gives the best result since it is within the experimental errors over the whole angular range considered. For the energy 40.9 MeV, the results of SFWS1 and SFWS3 are very similar and reproduce the data very well over the whole angular range. The difference between the results of SFWS1, 3 and those of SFWS2 starts at an angle of around 32° . For the energy 82.3 MeV, SFWS2, 3 potentials give very similar results and start to deviate from that of SFWS1 at angle of around 22° . For the other energies all the three sets give very similar results and reproduce the data nicely over the considered angular range. The experimental data of the analyzing power A_y are presented besides those of differential cross sections at the energy 71.0 MeV. This is considered as a good test for the considered potential. From Fig. 2 it is seen that the SFWS1 and SFWS3 results are near to reproduce the experimental data over the whole angular range, except for most backward data points of A_y at 71 MeV, more than those of SFWS2.

As another alternative for the imaginary potential, the folded potential is used and normalized by an imaginary normalization factor N_i . The spin-orbit potential is treated as usual by using the Thomas form. The calculations based on this imaginary folded potential are denoted as SFRI in Fig.3. The best fitting parameters of these calculations are collected in Table 3. It is found that a spin-orbit potential of shape parameters, $r_{\text{so}} = 1.362$ fm, $a_{\text{so}} = 0.786$ fm and of rms radius $\langle r_{\text{so}}^2 \rangle^{1/2} = 3.479$ fm, gives the best results. As observed in Fig. 3, the SFRI gives satisfactory results of $d\sigma/d\Omega$ over the considered energy range. For A_y , the results of SFRI are within the experimental errors except for the last two angles.

Finally, for consistency, the spin-orbit term is taken extracted from the SF potential as

$$V_{\text{so}}(R) = (N_{\text{rso}} + iN_{\text{iso}}) \frac{2}{R} \frac{dV(R)}{dR}, \quad (26)$$

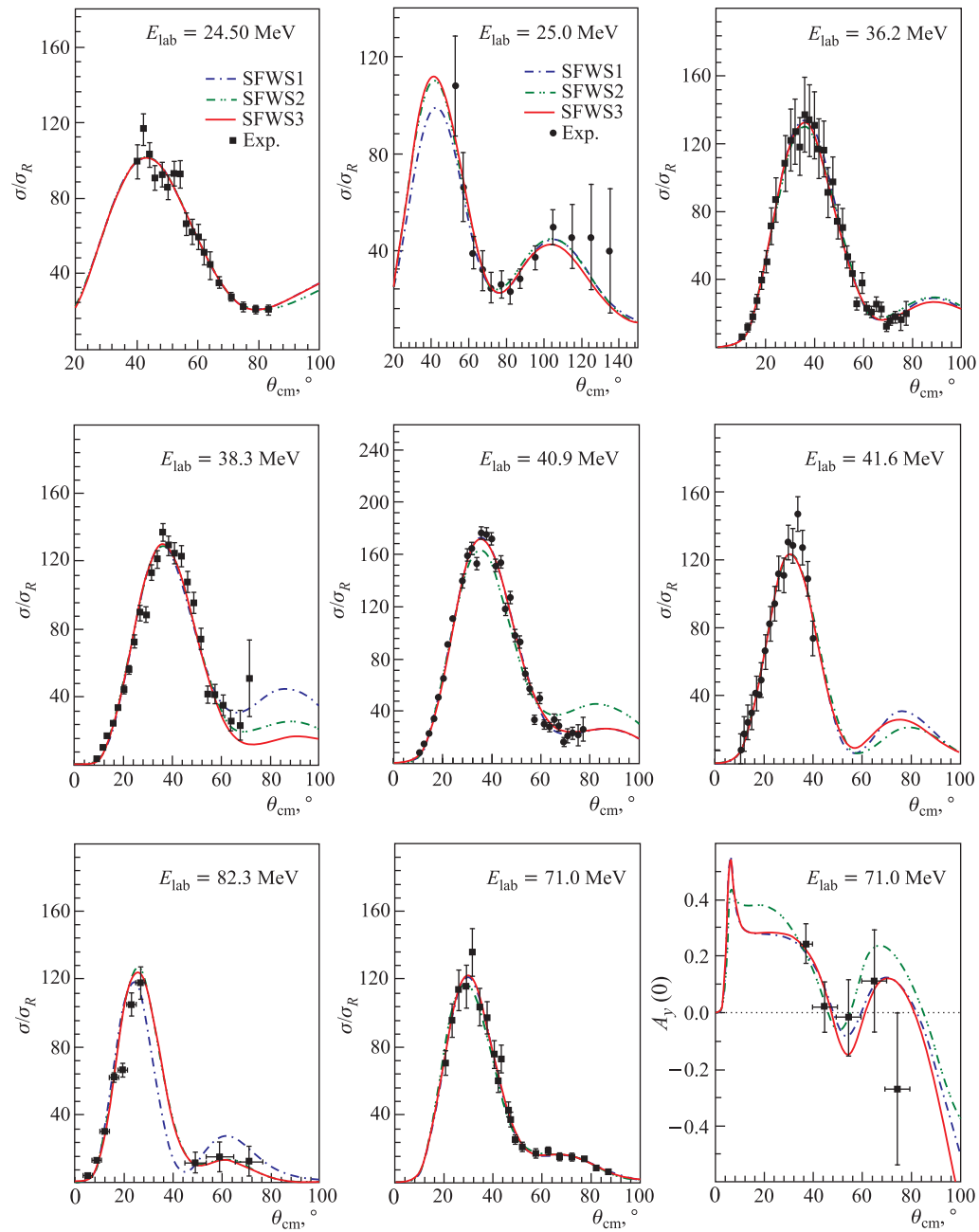


Fig. 2. Same as Fig. 1, but using the derived SF real potentials

Table 2. Phenomenological optical potential fitting parameters obtained using Eq. (23) for $p + {}^6\text{He}$ elastic scattering using WS central real and imaginary potentials and spin-orbit term of Thomas form. D_x and D_{xx} correspond to the depths of the potential (V_0 , W_{iv} , V_{so} and iW_{so}) and W_{is} , respectively. Same definition for radius and diffuseness parameters (R_x and a_x) in fm, real and imaginary volume integrals (J_x , $x = 0, I$ and So) in $\text{MeV} \cdot \text{fm}^3$, total reaction cross section (σ_R) in mb and rms radii $\langle r_x^2 \rangle^{1/2}$ in fm

E , MeV	Set	Poten- tial	D_x , MeV	D_{xx} , MeV	r_x , fm	a_x , fm	J_x , $\text{MeV} \cdot \text{fm}^3$	$\langle r_x^2 \rangle^{1/2}$, fm	σ_R , mb	
24.5	Set-1	Real	37.303	—	1.115	0.690	467.2	3.003	414.5	
		Imag.	14.374	5.317	0.850	0.719	245.7	3.084		
		Re-SO	2.154	—	1.248	0.910	21.11	3.612		
	Set-2	Real	39.212	—	1.455	1.053	408.7	2.907		
		Imag.	16.422	0.584	1.298	1.500	205.4	3.621		
		Re-SO	3.977	—	1.248	0.910	38.98	3.612		
	Set-3	Real	45.64	—	1.455	1.053	475.7	2.907		421.3
		Imag.	11.507	2.971	1.455	1.053	243.7	3.145		
		Re-SO	2.459	—	1.301	1.032	25.38	3.964		
25.0	Set-1	Real	39.153	—	1.115	0.690	490.4	3.003	428.6	
		Imag.	18.957	4.635	0.850	0.719	267.3	3.052		
		Re-SO	0.279	—	1.248	0.910	2.738	3.612		
	Set-2	Real	43.577	—	1.455	1.053	454.2	2.907		434.6
		Imag.	16.652	1.024	1.298	1.500	230.3	3.657		
		Re-SO	0.775	—	1.248	0.910	7.600	3.612		
	Set-3	Real	45.64	—	1.455	1.053	475.7	3.907		417.7
		Imag.	11.715	2.918	1.455	1.053	243.6	3.140		
		Re-SO	2.459	—	1.301	1.032	25.38	3.964		
36.2	Set-1	Real	39.615	—	1.115	0.690	496.2	3.003	404.0	
		Imag.	3.988	10.988	0.850	0.719	295.6	3.198		
		Re-SO	0.133	—	1.248	0.910	1.307	3.612		
	Set-2	Real	40.366	—	1.455	1.053	420.7	2.907		383.6
		Imag.	17.499	1.078	1.298	1.500	242.6	3.657		
		Re-SO	2.500	—	1.248	0.910	25.50	3.612		
	Set-3	Real	40.322	—	1.455	1.053	420.3	2.907		330.0
		Imag.	11.559	2.463	1.455	1.053	223.1	3.123		
		Re-SO	2.459	—	1.301	1.032	25.38	3.964		
38.3	Set-1	Real	38.826	—	1.115	0.690	486.3	3.003	366.0	
		Imag.	32.206	0.799	0.850	0.719	284.9	2.941		
		Re-SO	0.197	—	1.248	0.910	1.926	3.612		
	Set-2	Real	41.632	—	1.455	1.053	433.9	2.907		309.8
		Imag.	23.251	-1.105	1.298	1.500	190.0	3.418		
		Re-SO	0.544	—	1.248	0.910	5.332	3.612		
	Set-3	Real	40.322	—	1.455	1.053	420.3	2.907		330.0
		Imag.	11.559	2.463	1.455	1.053	223.1	3.123		
		Re-SO	2.459	—	1.301	1.032	25.38	3.964		
Set-3	Im-SO	1.163	—	1.301	1.032	12.00	3.964			

The end of Table 2

E , MeV	Set	Poten- tial	D_x , MeV	D_{xx} , MeV	r_x , fm	a_x , fm	J_x , MeV · fm ³	$\langle r_x^2 \rangle^{1/2}$, fm	σ_R , mb
40.9	Set-1	Real	39.494	—	1.115	0.690	494.7	3.003	322.7
		Imag.	-4.650	10.505	0.850	0.719	212.8	3.284	
		Re-SO	1.334	—	1.248	0.910	13.08	3.612	
	Set-2	Real	44.193	—	1.455	1.053	460.6	2.907	308.8
		Imag.	0.766	3.318	1.298	1.500	181.2	3.958	
		Re-SO	0.093	—	1.248	0.910	0.914	3.612	
	Set-3	Real	45.922	—	1.455	1.053	478.7	2.907	300.2
		Imag.	7.007	2.875	1.455	1.053	192.8	3.195	
		Re-SO	2.459	—	1.301	1.032	25.38	3.964	
41.6	Set-1	Real	35.434	—	1.115	0.690	443.8	3.003	496.9
		Imag.	-3.265	22.329	0.850	0.719	506.9	3.246	
		Re-SO	5.491	—	1.248	0.910	53.82	3.612	
	Set-2	Real	43.538	—	1.455	1.053	453.8	2.907	494.2
		Imag.	40.050	-0.006	1.298	1.500	426.2	3.556	
		Re-SO	6.428	3.019	1.248	0.910	63.00	3.612	
	Set-3	Real	41.781	—	1.455	1.053	435.5	2.907	370.8
		Imag.	11.559	3.875	1.455	1.053	281.8	3.174	
		Re-SO	2.459	—	1.301	1.032	25.38	3.964	
71.0	Set-1	Real	24.991	—	1.115	0.690	313.0	3.003	194.7
		Imag.	23.243	-1.068	0.850	0.719	166.3	2.868	
		Re-SO	2.643	—	1.248	0.910	25.90	3.612	
	Set-2	Real	28.808	—	1.455	1.053	300.3	2.907	148.8
		Imag.	31.918	-4.239	1.298	1.500	118.9	2.602	
		Re-SO	3.054	—	1.248	0.910	29.93	3.612	
	Set-3	Real	29.626	—	1.455	1.053	308.8	2.907	120.3
		Imag.	11.583	-0.737	1.455	1.053	90.04	2.735	
		Re-SO	2.459	—	1.301	1.032	25.38	3.964	
82.3	Set-1	Real	23.666	—	1.115	0.690	296.4	3.003	286.5
		Imag.	41.157	-0.469	0.850	0.719	328.5	2.907	
		Re-SO	2.500	—	1.248	0.910	24.50	3.612	
	Set-2	Real	30.217	—	1.455	1.053	315.0	2.907	293.4
		Imag.	53.275	-4.987	1.298	1.500	307.3	3.158	
		Re-SO	0.241	—	1.248	0.910	2.360	3.612	
	Set-3	Real	28.081	—	1.455	1.053	292.7	2.907	230.8
		Imag.	8.773	2.875	1.455	1.053	211.2	3.171	
		Re-SO	2.459	—	1.301	1.032	25.38	3.964	
		Im-SO	1.163	—	1.301	1.032	12.00	3.964	

where the form $F_{so}(R)$ is replaced by the folded potential given by Eq. (1) and the real and imaginary depths V_{so} and W_{so} are replaced with the normalization factors N_{rso} and N_{iso} , respectively. By using this procedure, the total optical potential takes the form

$$U_{op}(R) = -(N_r + N_i) V(R) + (N_{rso} + iN_{iso}) \frac{2}{R} \frac{dV(R)}{dR} + U_c(R). \quad (27)$$

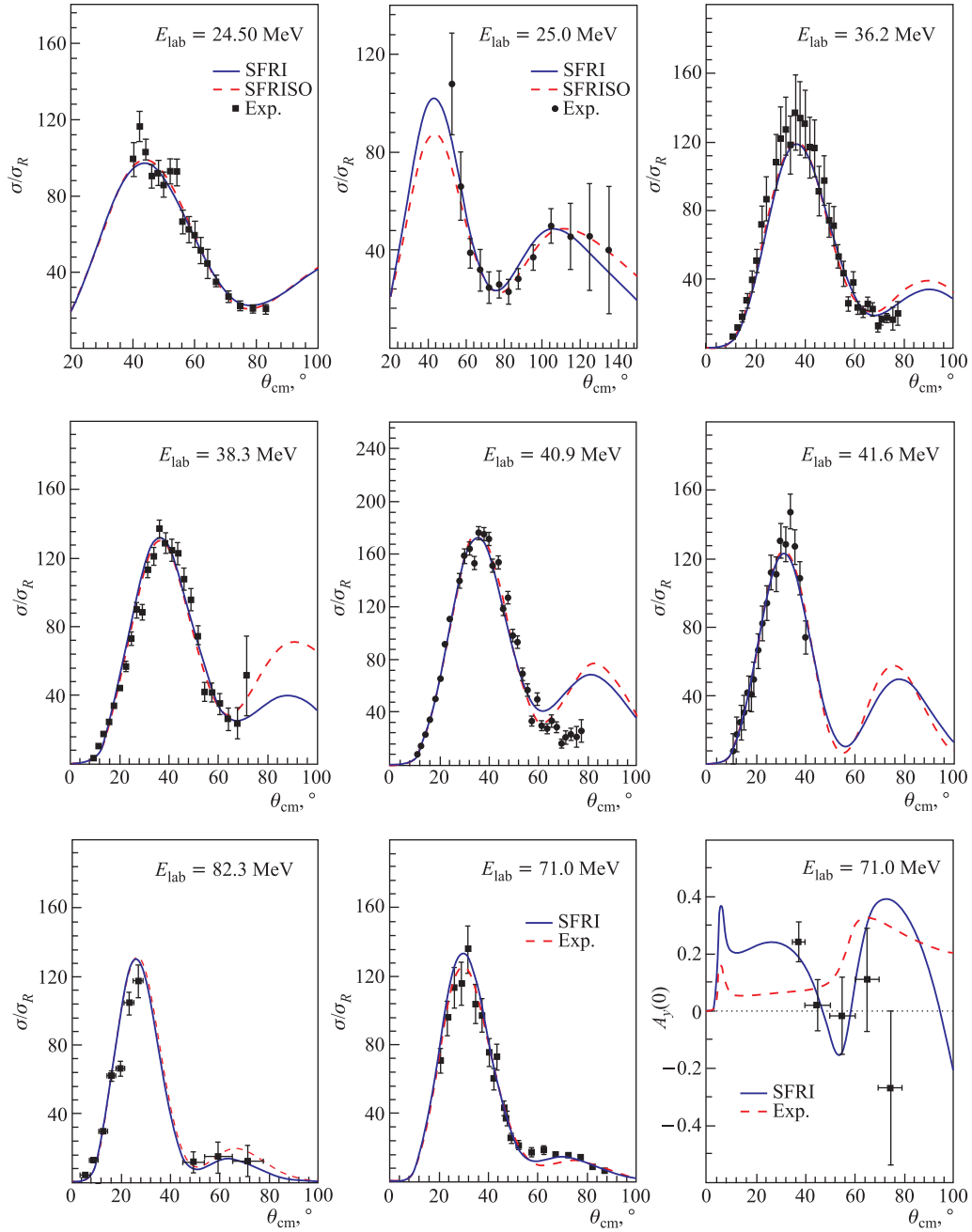


Fig. 3. Same as Fig. 1, but for the derived complex potentials

Table 3. Optical model best fit parameters for $p + {}^6\text{He}$ elastic scattering using central real folded and WS imaginary potentials with spin-orbit term of Thomas form

E , MeV	Poten- tial	N_r	W_i , MeV	W_D , MeV	W_{sr} , MeV	W_{si} , MeV	J_r , MeV · fm ³	J_i , MeV · fm ³	J_{sr} , MeV · fm ³	J_{si} , MeV · fm ³	σ_R , mb
24.5	SFWS1	1.088	14.193	5.426	4.044	1.059	466.5	259.9	39.64	10.38	429.8
	SFWS2	1.034	15.716	2.038	4.512	1.608	443.4	240.8	41.66	14.85	432.4
	SFWS3	1.069	22.319	0.708	1.533	0.827	458.3	243.9	15.02	8.110	430.2
25.0	SFWS1	1.163	23.406	3.153	0.141	0.002	497.7	282.6	1.386	0.0152	440.9
	SFWS2	1.178	17.492	2.230	0.108	-0.001	504.0	266.3	0.995	-0.0013	460.9
	SFWS3	1.175	11.367	3.583	0.205	0.452	502.7	268.8	2.007	4.432	469.3
36.2	SFWS1	1.190	4.242	10.582	2.518	1.017	490.6	303.6	24.68	9.971	412.8
	SFWS2	1.136	16.656	2.555	0.924	0.157	468.4	273.0	8.530	1.453	404.3
	SFWS3	1.127	7.921	4.365	2.266	1.067	464.5	271.1	22.21	10.45	409.7
38.3	SFWS1	1.193	33.152	0.122	0.745	0.968	488.1	290.7	7.304	9.483	371.8
	SFWS2	1.044	14.572	1.294	2.500	2.335	427.5	230.4	23.08	21.56	348.6
	SFWS3	1.000	0.172	4.709	0.861	1.366	409.4	212.9	8.435	13.39	342.3
40.9	SFWS1	1.215	-5.644	10.784	1.160	1.642	492.7	222.9	11.37	16.09	332.0
	SFWS2	1.218	15.000	1.648	2.500	0.009	494.2	216.5	23.08	0.085	334.0
	SFWS2	1.123	-8.893	6.070	2.127	0.356	455.7	187.8	20.85	3.493	312.9
41.6	SFWS1	1.109	5.223	17.988	6.028	1.004	448.8	498.8	59.08	9.835	496.7
	SFWS2	1.187	17.861	5.670	1.670	-0.118	480.4	424.2	15.42	-1.093	497.5
	SFWS3	1.085	28.178	3.667	7.175	1.739	439.0	432.4	70.32	17.05	489.0
71.0	SFWS1	0.780	13.241	-1.587	4.294	0.291	283.4	74.88	42.09	2.855	103.5
	SFWS2	0.841	39.927	-5.018	3.578	-0.034	305.6	154.4	33.04	-0.317	177.0
	SFWS3	0.783	24.332	-3.282	4.276	0.527	284.3	84.01	41.91	5.167	110.9
82.3	SFWS1	0.949	-24.58	20.631	0.318	0.885	329.8	306.8	3.116	8.676	313.1
	SFWS2	0.883	68.706	-6.876	-0.279	0.198	306.6	344.5	-2.575	1.830	293.4
	SFWS3	0.854	68.027	-6.844	0.947	0.231	296.6	339.5	9.282	2.266	290.2

The parameters N_r , N_i , N_{rso} and N_{iso} are treated as variational parameters to reproduce the experimental cross section. The results of this procedure are denoted as SFRISO and shown by dashed line. The best fitting parameters obtained are collected in Table 5. The rms radius of the obtained spin-orbit potential using Eq.(25) at the energy 71.0 MeV is 3.061 fm. Comparing this value with that obtained using spin-orbit potential of phenomenological Thomas form, we note that the spin-orbit potential of Eq. (25) has a shorter range. So, to reproduce the experimental data by using this procedure, a correction term should be added to the folded spin-orbit potential [12, 35]. Also, a correction term could be added at least to the imaginary folded potential to simulate this effect.

It is commonly surmised that, because ${}^6\text{He}$ is weakly bound, breakup has a large effect on the elastic scattering channel and is responsible for the reduction of N_r below unity. This effect can be represented by a dynamic polarization potential (DPP) which has a strongly repulsive real part in the surface and an additional absorptive (imaginary) part [42]. If the contribution from the DPP were simulated by a surface correction using splines added to both the M3Y and DDM3Y real DF potentials, Khoa et al. [42] could obtain successful descriptions of the ${}^6\text{Li} + {}^{12}\text{C}$ elastic scattering data without using a normalizing factor, i.e., $N_R = 1$, all over the energy range $E = 10\text{--}53$ MeV/nucleon.

Table 4. Optical model fitting parameters for $p + {}^6\text{He}$ elastic scattering using central folded real and imaginary potentials with spin-orbit term of Thomas form

E , MeV	N_r	N_i	W_{sr} , MeV	W_{si} , MeV	J_r , MeV · fm ³	J_i , MeV · fm ³	J_{sr} , MeV · fm ³	J_{si} , MeV · fm ³	σ_R , mb
24.5	1.089	0.610	3.315	0.131	467.1	261.4	34.83	1.381	418.1
25.0	1.098	0.649	7.159	3.802	470.0	277.7	75.21	39.94	418.6
36.2	1.068	0.698	3.130	0.401	440.3	287.6	32.88	4.214	377.1
38.3	1.163	0.672	0.588	0.771	476.0	275.1	6.176	8.101	363.9
40.9	1.151	0.564	7.715	0.457	466.8	228.9	81.05	4.804	323.4
41.6	1.364	1.433	2.416	1.724	551.8	580.0	25.38	18.11	499.1
71.0	0.859	0.161	2.744	-0.335	312.0	58.39	28.82	-3.517	84.77
82.3	0.978	0.573	3.338	0.905	339.8	199.0	30.82	8.357	218.7

Table 5. Optical model best fit parameters for $p + {}^6\text{He}$ elastic scattering using central folded real, imaginary and spin-orbit potentials

E , MeV	N_r	N_i	N_{rso}	N_{iso}	J_r , MeV · fm ³	J_i , MeV · fm ³	J_{rso} , MeV · fm ³	J_{iso} , MeV · fm ³	σ_R , mb
24.5	0.981	0.661	0.382	0.053	420.7	283.5	121.5	16.79	431.6
25.0	1.178	0.970	0.220	0.329	504.0	415.3	69.68	104.3	449.4
36.2	1.180	0.792	0.009	-0.004	486.6	326.5	2.687	-1.135	405.5
38.3	1.259	1.383	0.271	0.501	515.5	566.1	79.29	146.6	407.2
40.9	1.046	0.762	0.541	0.119	424.4	308.9	155.7	34.20	379.0
41.6	1.039	1.731	0.542	0.342	420.4	700.5	155.4	97.92	499.6
71.0	0.871	0.170	0.077	0.004	316.4	61.76	17.87	1.003	90.20
82.3	0.973	0.664	0.023	0.128	337.8	230.7	4.803	27.11	231.8

The obtained total reaction cross sections, σ_R , listed in Tables 2–4 for both the phenomenological and microscopic calculations are compared with only one available experimental value measured at 36.2 MeV/nucleon, (410 ± 21) mb [22, 44]. In general, σ_R decreases almost linearly as energy increases. It is clear that the values of σ_R corresponding to the SF calculations are more consistent with the measured value than the corresponding value related to the WS one. Unfortunately, no other reported values of σ_R , at the energy range considered in this work, in previous studies are found to be compared with our results.

From this calculation it is expected that the addition of surface imaginary potential to the volume folded one may give better results than those obtained.

CONCLUSIONS

The SF optical potentials are generated based on the deduced density and the BDM3Y1 effective NN interaction. Eight sets of $p + {}^6\text{He}$ elastic scattering data at energies of 24.5, 25.0, 36.2, 38.3, 40.9, 41.6, 71.0 and 82.3 MeV are analyzed using both the derived real potentials and the phenomenological WS potentials in the framework of the DWBA mechanism. Successful reproductions of the data are obtained using the generated potentials. From the present analysis it is clear that the optical potential of $p + {}^6\text{He}$ is very ambiguous. Also,

from the variation of the depths of volume real, imaginary and surface imaginary potentials in phenomenological analysis, it is clear that introducing the effect of DPP potential is recommended. This effect is also clear through the variation of the normalization factors when the folded model is used to get the real or the imaginary parts of the optical potential. This analysis also shows that a spin-orbit potential with large diffuseness and long range is needed to reproduce the analyzing power data A_y at 71 MeV. This may resemble the diffuse density of the neutron-rich ${}^6\text{He}$ nucleus. It is also recommended that the vector analyzing power should be measured along with the differential cross sections to get an optical potential maybe free of ambiguities, since the vector analyzing power adds another constraint on the considered optical potential.

Finally, the present work confirmed the success of the SF model based upon the BDM3Y1 effective NN interaction to produce successful predictions of the $p + {}^6\text{He}$ elastic scattering data at intermediate energies.

REFERENCES

1. *Tanihata I. et al.* Measurements of Interaction Cross Sections and Nuclear Radii in the Light p -Shell Region // *Phys. Rev. Lett.* 1985. V. 55. P. 2676;
Tanihata I. et al. Measurements of Interaction Cross Sections and Radii of He Isotopes // *Phys. Lett. B.* 1985. V. 160. P. 380;
Tanihata I. et al. Measurement of Interaction Cross Sections Using Isotope Beams of Be and B and Isospin Dependence of the Nuclear Radii // *Phys. Lett. B.* 1988. V. 206. P. 592;
Tanihata I. et al. Determination of the Density Distribution and Correlation of Halo Neutrons in ${}^{11}\text{Li}$ // *Phys. Lett. B.* 1992. V. 287. P. 307;
Tanihata I. Neutron Halo Nuclei // *J. Phys. G.* 1996. V. 22. P. 157.
2. *Gupta R. K. et al.* The Cluster-Core Model for the Halo Structure of Light Nuclei at the Drip Lines // *J. Phys. G: Nucl. Part. Phys.* 2002. V. 28. P. 699.
3. *Hansen P. G., Jensen A. S., Jonson B.* Nuclear Halos // *Ann. Rev. Nucl. Part. Sci.* 1995. V. 45. P. 591 and references therein.
4. *Jonson B., Riisager K.* Halo and Halo Excitations // *Philos. Trans. R. Soc. A.* 1998. V. 356. P. 323.
5. *Tanihata I.* RI Beams Dream and Reality // *Nucl. Phys. A.* 2001. V. 685. P. 80c and references therein.
6. *Bhagwat A., Gambhir Y. K., Patil S. H.* Nuclear Densities in the Neutron-Halo Region // *Eur. Phys. J. A.* 2000. V. 8. P. 511.
7. *Blackmon J. C. et al.* Elastic Scattering of the Proton Drip-Line Nucleus ${}^{17}\text{F}$ // *Phys. Rev. C.* 2005. V. 72. P. 034606.
8. *El-Azab Farid M., Nossair A. M. A., Ibraheem Awad A.* Folding Model Analysis of ${}^6\text{He} + {}^{12}\text{C}$ Elastic Scattering // *Intern. J. Mod. Phys. E.* 2008. V. 174. P. 715.
9. *Ibraheem Awad A. et al.* Folding Model Description of Reactions with Exotic Nuclei // *Phys. At. Nucl.* 2012. V. 75. P. 969.
10. *Signorini C. et al.* Interaction of ${}^{17}\text{F}$ with a ${}^{208}\text{Pb}$ Target below the Coulomb Barrier // *Eur. Phys. J. A.* 2010. V. 44. P. 63.
11. *Mohr P. et al.* Comparison of ${}^{120}\text{Sn}({}^6\text{He}, {}^6\text{He}){}^{120}\text{Sn}$ and ${}^{120}\text{Sn}(\alpha, \alpha){}^{120}\text{Sn}$ Elastic Scattering and Signatures of the ${}^6\text{He}$ Neutron Halo in the Optical Potential // *Phys. Rev. C.* 2010. V. 82. P. 044606.
12. *Sakaguchi S. et al.* Analyzing Power in Elastic Scattering of ${}^6\text{He}$ from a Polarized Proton Target at 71 MeV/nucleon // *Phys. Rev. C.* 2011. V. 84. P. 024604.

13. Neumaier S.R. et al. Small-Angle Proton Elastic Scattering from the Neutron-Rich Isotopes ${}^6\text{He}$ and ${}^8\text{He}$, and from ${}^4\text{He}$, at 0.7 GeV in Inverse Kinematics // Nucl. Phys. A. 2002. V. 712. P. 247.
14. Alkhazov G.D. et al. Nuclear Matter Distributions in ${}^6\text{He}$ and ${}^8\text{He}$ from Small Angle p -He Scattering in Inverse Kinematics at Intermediate Energy // Phys. Rev. Lett. 1997. V. 78. P. 2313.
15. Crespo R., Moro A.M. Polarization Observables in the Elastic Scattering of Protons from ${}^{4,6,8}\text{He}$ // Phys. Rev. C. 2007. V. 76. P. 054607.
16. Ter-Akopian G.M. et al. Two-Neutron Exchange Observed in the ${}^6\text{He} + {}^4\text{He}$ Reaction. Search for the «Di-neutron» Configuration of ${}^6\text{He}$ // Phys. Lett. B. 1998. V. 426. P. 251.
17. Wolski R. et al. JINR Report E15-98-284. Dubna, 1998.
18. Korshenimikov A.A. et al. Scattering of Radioactive Nuclei ${}^6\text{He}$ and ${}^3\text{H}$ by Protons: Effects of Neutron Skin and Halo in ${}^6\text{He}$, ${}^8\text{He}$, and ${}^{11}\text{Li}$ // Nucl. Phys. A. 1997. V. 617. P. 45.
19. Cortina-Gil M.D. et al. Search for the Signature of a Halo Structure in the $p({}^6\text{He}, {}^6\text{Li})n$ Reaction // Phys. Lett. B. 1996. V. 14. P. 371.
20. Lagoyannis A. et al. Probing the ${}^6\text{He}$ Halo Structure with Elastic and Inelastic Proton Scattering // Phys. Lett. B. 2001. V. 518. P. 27.
21. Lapoux V. et al. Coupling Effects in the Elastic Scattering of the Exotic Nucleus ${}^6\text{He}$ on Protons // Ibid. V. 517. P. 18.
22. de Vismes A. et al. A Determination of the ${}^6\text{He} + p$ Interaction Potential // Ibid. V. 505. P. 15.
23. Wolski R. et al. Cluster Structure of ${}^6\text{He}$ Studied by Means of ${}^6\text{He} + p$ Reaction at 25 MeV/nucleon Energy // Phys. Lett. B. 1999. V. 467. P. 8.
24. Stepantsov S.V. et al. 24.5A MeV ${}^6\text{He} + p$ Elastic and Inelastic Scattering // Phys. Lett. B. 2002. V. 542. P. 35.
25. Abu-Ibrahim B., Fujimura K., Suzuki Y. Calculation of the Complete Glauber Amplitude for $p + {}^6\text{He}$ Scattering // Nucl. Phys. A. 1999. V. 657. P. 391.
26. Alkhazov G.D. et al. Nuclear Matter Distributions in the ${}^6\text{He}$ and ${}^8\text{He}$ Nuclei from Differential Cross Sections for Small-Angle Proton Elastic Scattering at Intermediate Energy // Nucl. Phys. A. 2002. V. 712. P. 269.
27. Gupta D., Samanta C., Kanungo R. Consistent Analysis of Proton Elastic Scattering from ${}^{4,6,8}\text{He}$ and ${}^{6,7,9,11}\text{Li}$ in the Energy Range of 25–75A MeV // Nucl. Phys. A. 2000. V. 674. P. 77.
28. Avrigeanu M. et al. Dynamics of Two-Neutron Transfer Reactions on the Borromean Nucleus ${}^6\text{He}$ Reexamined // Phys. Rev. C. 2000. V. 62. P. 017001.
29. Satchler G.R. // Proc. of the Intern. Conf. on Reactions between Complex Nuclei, Nashville, Tennessee, 1974. P. 171.
30. Gupta D., Samanta C. Inelastic Scattering of Protons from ${}^{6,8}\text{He}$ and ${}^{7,11}\text{Li}$ in a Folding Model Approach // J. Phys. G. 2002. V. 28. P. 85.
31. Hatano M. et al. First Experiment of ${}^6\text{He}$ with a Polarized Proton Target // Eur. Phys. J. A. 2005. V. 25. P. 255.
32. Weppner S.P., Garcia O., Elster Ch. Sensitivities of the Proton–Nucleus Elastic Scattering Observables of ${}^6\text{He}$ and ${}^8\text{He}$ at Intermediate Energies // Phys. Rev. C. 2000. V. 61. P. 044601.
33. Crespo R., Moro A.M. Polarization Observables in the Elastic Scattering of Protons from ${}^{4,6,8}\text{He}$ // Phys. Rev. C. 2007. V. 76. P. 054607.
34. Karataglidis S., Kim Y.J., Amos K. Nucleon–Nucleus Scattering as a Test of Shell Structure of Some Light Mass Exotic Nuclei // Nucl. Phys. A. 2007. V. 793. P. 40;
Lukyanov K.V. et al. // Eur. Phys. J. A. 2007. V. 33. P. 389.
35. Uesaka T. et al. Analyzing Power for Proton Elastic Scattering from the Neutron-Rich ${}^6\text{He}$ Nucleus // Phys. Rev. C. 2010. V. 82. P. 021602(R).

36. *Satchler G.R., Love W.G.* Folding Model Potentials from Realistic Interactions for Heavy-Ion Scattering // *Phys. Rep.* 1979. V. 55. P. 183.
37. *Khoa Dao T., von Oertzen W., Ogloblin A. A.* Study of the Equation of State for Asymmetric Nuclear Matter and Interaction Potential between Neutron-Rich Nuclei Using the Density-Dependent M3Y Interaction // *Nucl. Phys. A.* 1996. V. 602. P. 98.
38. *Basu D.N., Chowdhury P. Roy, Samanta C.* Folding Model Analysis of Proton Radioactivity of Spherical Proton Emitters // *Phys. Rev. C.* 2005. V. 72. P. 051601(R).
39. *Khoa Dao T.* Exchange Effects in Nuclear Rainbow Scattering // *Nucl. Phys. A.* 1988. V. 484. P. 376.
40. *Abu-Ibrahim B., Suzuki Y.* The Optical Potential of ${}^6\text{He}$ in the Eikonal Approximation // *Nucl. Phys. A.* 2003. V. 728. P. 118; Erratum // *Nucl. Phys. A.* 2004. V. 732. P. 218.
41. *Cook J.* Hermes — an Optical Model Search Program Including Tensor Potentials for Projectile Spins 0 to 3/2 // *Comp. Phys. Commun.* 1984. V. 31. P. 363.
42. *Jamil-Qureshi Faisal et al.* Elastic Scattering of ${}^6\text{He} + p$ at 82.3 MeV/nucleon // *Chin. Phys. Lett.* 2010. V. 27, No. 9. P. 092501.
43. *Khoa D.T., Satchler G.R., von Oertzen W.* Folding Analysis of the Elastic ${}^6\text{Li} + {}^{12}\text{C}$ Scattering: Knock-on Exchange Effects, Energy Dependence, and Dynamical Polarization Potential // *Phys. Rev. C.* 1995. V. 51. P. 2069 and references therein.
44. *de Vismes A. et al.* Proton Reaction Cross-Section Measurements on Stable and Neutron-Rich Nuclei as a Probe of the Nucleon–Nucleus Interaction // *Nucl. Phys. A.* 2003. V. 706. P. 295.

Received on August 5, 2013.